Forsch Ingenieurwes (2019) 83:491–507
https://doi.org/10.1007/s10010-019-00365-2

ORIGINALARBEITEN/ORIGINALS

Dynamic Modeling and Analysis of a Star-wheel Reducer

Jian Wang[1] · **Jun Zhang**[1]

Received: 29 March 2019 / Accepted: 11 July 2019

Abstract
The star-wheel reducer has been regarded as a promising alternative solution for industrial power transmission where large transmission ratio and high power density are required. As one of the most overwhelming concerns in the early design stage of such kind of transmission device, its dynamic performance must be evaluated in advance to provide guidelines for vibration suppression and tolerance control. For this purpose, this paper proposes a methodology of dynamic modeling for the star-wheel reducer and analyzes the dynamic behaviors of the transmission system. By using the technique of substructure synthesis, an analytical elasto-dynamic model is established in which the effects of component compliances and manufacturing/assembling errors are included. The differential motion equations of each subsystem are derived with the 2nd Newtonian law. These differential motion equations are further assembled by the compatibility conditions among the subsystems to formulate a governing equation of the overall transmission system. Based on the established dynamic model, a modal analysis and a dynamic analysis are carried out to reveal the modal characteristics and the steady-state responses of the star-wheel reducer. The results show that the first 6 orders natural frequencies are ranging from 66.2 to 197 Hz and are much higher than the reducer's input frequency of 16.7 Hz under input speed of 1000 r/min. In addition, the meshing forces of the two phases of star-wheel are similar only with a phase difference of 180°. Finally, a test-rig is set up to perform an experimental modal test and a vibration test. The satisfactory agreement between the experimental data and the theoretical simulation results proves the correctness and accuracy of the proposed dynamic model. The present study is expected to provide a fundamental framework for error controlling and performance enhancement of the star-wheel reducer.

✉ Jun Zhang
zhang_jun@fzu.edu.cn

[1] School of Mechanical Engineering and Automation, Fuzhou University, 350116 Fuzhou, China

Dynamische Modellierung und Analyse eines Sternradgetriebes

Zusammenfassung

Das Sternradgetriebe gilt als vielversprechende Alternative für die industrielle Kraftübertragung, bei der große Übersetzungsverhältnisse und eine hohe Leistungsdichte gefordert sind. Als eines der überwältigendsten Anliegen in der frühen Entwurfsphase eines solchen Getriebegeräts muss dessen dynamisches Verhalten im Voraus bewertet werden, um Richtlinien für die Unterdrückung von Vibrationen und die Toleranzkontrolle bereitzustellen. Zu diesem Zweck wird in diesem Artikel eine Methodik zur dynamischen Modellierung des Sternradgetriebes vorgeschlagen und das dynamische Verhalten des Getriebesystems analysiert. Unter Verwendung der Technik der Substruktursynthese wird ein analytisches elastodynamisches Modell erstellt, in das die Auswirkungen von Bauteilübereinstimmungen und Fertigungs- / Montagefehlern einbezogen werden. Die Differentialbewegungsgleichungen jedes Subsystems werden mit dem 2. Newtonschen Gesetz abgeleitet. Diese Differentialbewegungsgleichungen werden ferner durch die Kompatibilitätsbedingungen zwischen den Teilsystemen zusammengesetzt, um eine maßgebliche Gleichung des gesamten Übertragungssystems zu formulieren. Basierend auf dem etablierten dynamischen Modell werden eine Modalanalyse und eine dynamische Analyse durchgeführt, um die Modaleigenschaften und die stationären Reaktionen des Untersetzungsgetriebes aufzudecken. Die Ergebnisse zeigen, dass die Eigenfrequenzen der ersten 6 Ordnungen im Bereich von 66.2 bis 197 Hz liegen und viel höher sind als die Eingangsfrequenz des Reduzierers von 16.7 Hz bei einer Eingangsgeschwindigkeit von 1000 r/min. Außerdem sind die Eingriffskräfte der beiden Phasen des Sternrades nur mit einer Phasendifferenz von 180° ähnlich. Schließlich wird ein Prüfstand eingerichtet, um einen experimentellen Modaltest und einen Vibrationstest durchzuführen. Die zufriedenstellende Übereinstimmung zwischen den experimentellen Daten und den theoretischen Simulationsergebnissen beweist die Richtigkeit und Genauigkeit des vorgeschlagenen dynamischen Modells. Die vorliegende Studie soll einen grundlegenden Rahmen für die Fehlerkontrolle und Leistungssteigerung des Sternradgetriebes bieten.

1 Introduction

Planetary gear trains have been widely used in various power transmission systems due to their distinct merits of compact structure, high efficiency and excellent load capacity. In the past decades, abundant investigations have been conducted on the planetary gear trains, ranging from kinematic formulation to dynamic prediction [1–5]. However, studies on the planetary gear train with small tooth number difference are quite rare. As a typical planetary gear transmission device, the reducer with small tooth number difference claims some unique properties such as large transmission ratio, high power density. From the perspective of mechanics, the reducer with small tooth number difference belongs to the over-constrained mechanical system, in which there exists statical indetermination caused by virtual constraints. Because of its unique structural and mechanic properties, the dynamic behavior of a reducer with small tooth number difference is very different from that of an ordinary planetary gear train.

According to the author's literature survey, only a few papers studied structural design, dynamic modeling, modal characteristic, dynamic responses and other issues of the reducer with small tooth number difference. For example, Tsai et al. [6] proposed a conceptual design of a cycloid planetary gear reducer with two teeth number difference and then derived the equations of cycloid profile, tooth contact and specific sliding. Aimed at the problems of bearing premature fatigue and high level noise in the three-ring gear reducer, Yang and Zhang [7] developed an elasto-dynamic model considering the compliances of bearings, shafts and meshing gear teeth. Huang et al. [8] analyzed the natural frequencies and modal shapes of planetary gear apparatus based on the finite element method. Li et al. [9] established a nonlinear dynamic model and investigated the effects of modification coefficient, backlash and transmission error on the dynamic responses of the planetary drive with small teeth number difference. In addition, Shu [10]; Li; [11] and Dai [12] investigated the load sharing, the tooth contact and the lubrication performance of planetary drives with small tooth number difference, respectively.

Compared to the aforementioned several types of reducer with small tooth number difference, the star-wheel reducer has more evenly distributed star-wheel shafts to bear the planetary gear load, which can avoid premature failure of the planetary bearings. However, the introducing of more star-wheel shafts brings more virtual constrains into the transmission system. This makes the load sharing among different load-branches very complicated and the system's dynamic responses very sensitive to manufacturing/assembling errors. To the author's best knowledge, the dynamic performance of the star-wheel reducer has not been studied yet. Note that an in-depth understanding of the dynamics is very important for the design as well as the manufacturing of the star-wheel reducer. In view of this, an elasto-dynamic model for the star-wheel reducer is established in the present study. Based on the established model, a modal analysis and a dynamic analysis will be carried out to reveal the modal characteristics and the steady-state

responses of the star-wheel reducer. Finally, the dynamic analysis results will be verified through experimental tests.

2 Elasto-dynamic modeling structural descriptions

A star-wheel reducer is composed of an input shaft, an output shaft, a set of star-wheel shaft, two star-wheels, a ring gear, a set of bearings, eccentric sleeves and some other components. Its structural schematic diagram and a 3-D virtual prototype are shown in Fig. 1 (**a**) and (**b**), respectively. For the sake of clarity, Fig. 1 (**c**) presents the exploded diagram of the virtual prototype.

1-Output shaft; 2-Rear bearing of output shaft; 3-Front bearing of output shaft; 4-Flange; 5-Rear end cap; 6-Box; 7-Ring gear; 8-Front bearing of star-wheel shaft; 9-Left support; 10-Bearing of star-wheel shaft; 11-2nd phase star-wheel; 12-Star-wheel shaft; 13-Bearing of star-wheel; 14-1st phase star-wheel; 15-Support shaft; 16-Right support; 17-Rear bearing of input shaft; 18-Eccentric sleeve; 19-Front bearing of input shaft; 20-Input shaft; 21-Front end cap; 22-Small end cap.

The transmission path of the star-wheel reducer is described as the following: 1) The power is fed into the system through the input shaft, and then drives the star-wheel translation through the eccentric sleeve connected with the input shaft; 2) The translational star-wheel will engage with the ring gear, thus driving the ring gear to rotate; 3) Since the ring gear is connected with the output shaft, the power is output by the output shaft. It should be noted that there are two star-wheels in the reducer to avoid the dead angle problem of crank slider mechanism.

According to the above analysis, the technique of substructure synthesis is adopted to establish a dynamic model for the star-wheel reducer. To be specific, the star-wheel reducer is divided into four substructures, i.e., the output shaft subsystem, the input shaft subsystem, the star-wheel shaft subsystem and the star-wheel subsystem, respectively.

2.1 Motion equation of subsystems

2.1.1 Motion equation of the input shaft subsystem

The input shaft subsystem is composed of an input shaft and two eccentric sleeves. The eccentric sleeves are fixed to the input shaft through two keys with a 180° symmetrical layout. The force diagram of the input shaft subsystem is shown in Fig. 2.

As shown in Fig. 2, a coordinate system O_I-xyz is set at the mass center of the input shaft. Herein, the parameters a_1 and a_2 correspond to the distances of the front and the rear bearings on the input shaft from the coordinate origin to the bearing centers, respectively; a_3 and a_4 denote the distances from O_I to the 1st and the 2nd eccentric sleeves, respectively; g_I is the weight of the input shaft; f_{sx1}, f_{sy1}, f_{sx2}, f_{sy2}, f_{Ix1}, f_{Iy1} f_{Ix2} and f_{Iy2} are the reaction forces of bearings respectively; f_{e1} and f_{e2} are the centrifugal forces of the input shaft at the position of the i^{th} translation star-wheel.

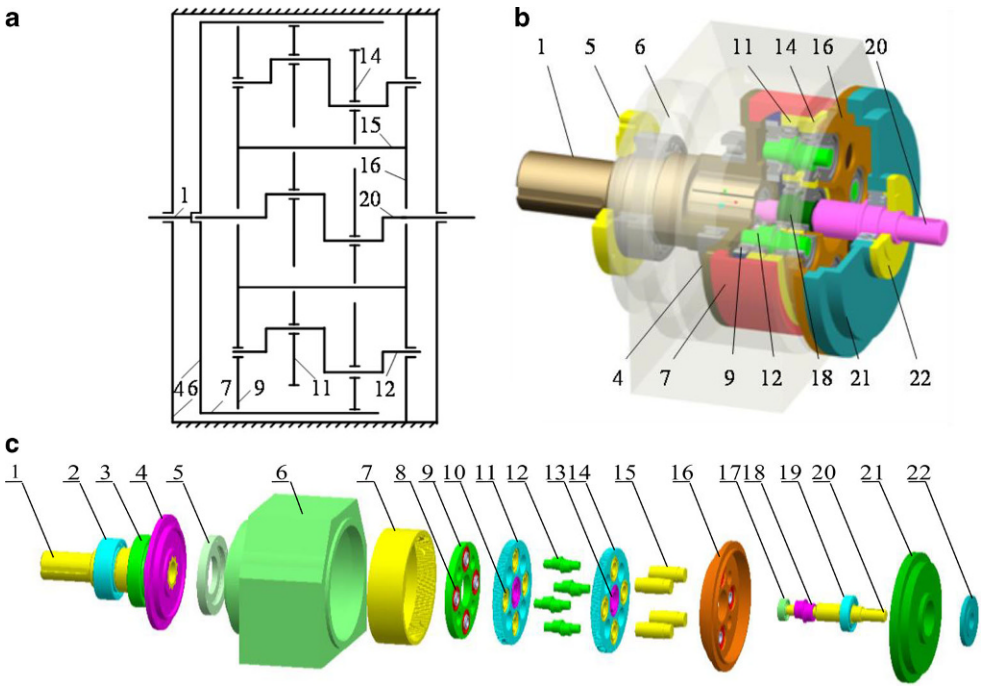

Fig. 1 Structure of a star-wheel reducer: (**a**) Schematic diagram of mechanism, (**b**) Three-dimensional assembly, (**c**) Exploded structure

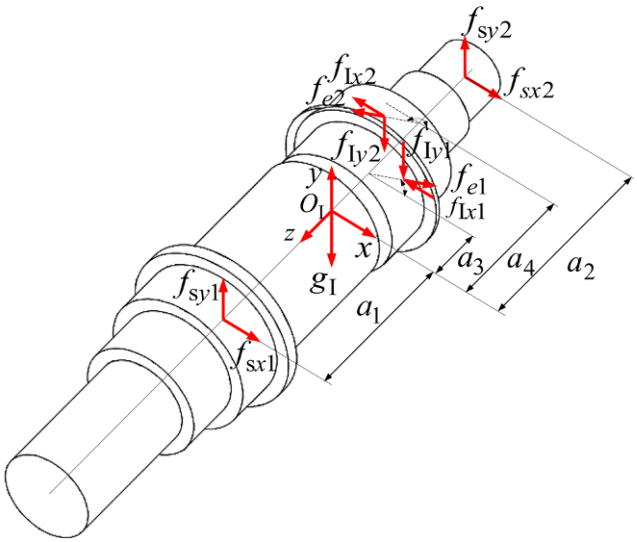

Fig. 2 Force diagram of the input shaft subsystem

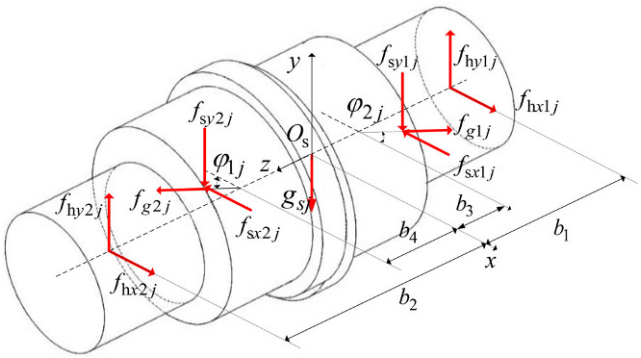

Fig. 3 Force diagram of the j^{th} star-wheel shaft subsystem

The motion equation of the input shaft subsystem can be formulated as

$$\begin{cases} m_I\ddot{x}_I = (f_{sx1} - f_{Ix1} + f_{ex1}) + (f_{sx2} - f_{Ix2} + f_{ex2}) \\ m_I\ddot{y}_I = (f_{sy1} - f_{Iy1} + f_{ey1}) + (f_{sy2} - f_{Iy2} + f_{ey2}) - g_I \\ j_{Ix}\ddot{\beta}_{Ix} = (-f_{sy1}a_1 - f_{Iy1}a_3 + f_{ey1}a_3) \\ +(f_{sy2}a_2 - f_{Iy2}a_4 - f_{ey2}a_4) \\ j_{Iy}\ddot{\beta}_{Iy} = (f_{sx1}a_1 + f_{Ix1}a_3 - f_{ex1}a_3) \\ +(f_{sx2}a_2 + f_{Ix2}a_4 + f_{ex2}a_4) \end{cases} \tag{1}$$

where m_I is the mass of the input shaft; j_{Ix} and j_{Iy} are the moment of inertia of the input shaft; f_{exi} and f_{eyi} are the centrifugal force components along x and y axes of the input shaft at the position of the i^{th} phase translational planet gear; x_I and y_I are the displacements of the input shaft; β_{Ix} and β_{Iy} are the angular displacements of the input shaft around x and y axes.

2.1.2 Motion equation of the star-wheel shaft subsystem

Taking the j^{th} star-wheel shaft as an example, its force diagram is shown in Fig. 3.

Herein, a coordinate system O_s-xyz is set at the mass center of the star-wheel shaft; the parameters b_1 and b_2 correspond to the distances of the front and the rear bearings on the star-wheel shaft from the coordinate origin to the bearing centers, respectively; the parameters b_3 and b_4 correspond to the distances from the coordinate origin to the gear centers of the 1st phase and the 2nd phase star-wheels respectively; φ_{1j} and φ_{2j} are the angles at which the crank rotates relative to x-axis; g_{sj} is the weight of the j^{th} star-wheel shaft; f_{hxij}, f_{hyij}, f_{sxij} and f_{syij} are the reaction forces of the bearings in x, y directions respectively; f_{gxij} and f_{gyij} are the component centrifugal force f_{gij} of the i^{th} star-wheel on the j^{th} star-wheel shaft along x and y directions.

The motion equation of the star-wheel shaft subsystem can be formulated as

$$\begin{cases} m_{sj}\ddot{x}_{sj} = (f_{hx1j} - f_{sx1j} + f_{gx1j}) \\ +(f_{hx2j} - f_{sx2j} + f_{gx2j}) \\ m_{sj}\ddot{y}_{sj} = (f_{hy1j} - f_{sy1j} + f_{gy1j}) \\ +(f_{hy2j} - f_{sy2j} + f_{gy2j}) - g_s \\ j_{sxj}\ddot{\beta}_{sxj} = -(f_{hy1j}b_1 - f_{sy1j}b_3 + f_{gy1j}b_3) \\ +(f_{hy2j}b_2 - f_{sy2j}b_4 + f_{gy2j}b_4) \\ j_{syj}\ddot{\beta}_{syj} = -(-f_{hx1j}b_1 + f_{sx1j}b_3 - f_{gx1j}b_3) \\ +(-f_{hx2j}b_2 + f_{sx2j}b_4 - f_{gx2j}b_4) \\ j_{szj}\ddot{\beta}_{szj} = e(f_{sx1j}\sin\varphi_{1j} - f_{sy1j}\cos\varphi_{1j}) \\ +e(f_{sx2j}\sin\varphi_{2j} - f_{sy2j}\cos\varphi_{2j}) \end{cases} \tag{2}$$

where m_{sj} is the mass of the j^{th} star-wheel shaft; j_{sxj}, j_{syj} and j_{szj} are the moments of inertia of the star-wheel shaft; x_{sj} and y_{sj} are the translational displacements of star-wheel shaft; β_{sxj}, β_{syj} and β_{szj} are the angular displacements of star-wheel shaft around x, y and z axes; e denotes eccentric distance of eccentric sleeve.

2.1.3 Motion equation of the star-wheel subsystem

The force diagram of the i^{th} phase star-wheel subsystem is shown in Fig. 4.

As shown in Fig. 4, O_i is the theoretical center of the i^{th} phase star-wheel; P_i is the pitch point; L is the distance from O_i to the star-wheel shaft hole; ϕ_j is the phase angle of the j^{th} star-wheel shaft; φ_i is the i^{th} phase crank angle; $\psi_i = \pi/2 - \alpha' + \varphi_i$, α' is the meshing angle, g_{pi} is the weight of the i^{th} phase star-wheel; f_{pi} is the centrifugal force of the i^{th} phase star-wheel.

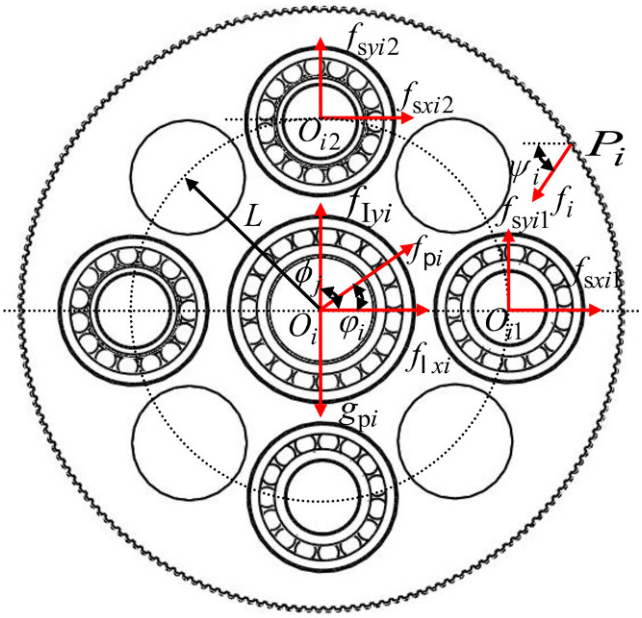

Fig. 4 Force diagram of the i^{th} phase star-wheel subsystem

The motion equation of the star-wheel subsystem can be formulated as

$$\begin{cases} m_{pi}\ddot{x}_{pi} = f_{Ixi} + \sum_{j=1}^{m} f_{sxij} - f_{xi} + f_{pxi} \\ m_{pi}\ddot{y}_{pi} = f_{Iyi} + \sum_{j=1}^{m} f_{syij} - f_{yi} + f_{pyi} - g_{pi} \\ j_{pzi}\ddot{\theta}_{pi} = \sum_{j=1}^{m} \left(f_{syij} L\cos\phi_j - f_{sxij} L\sin\phi_j \right) - f_i r_{bp} \end{cases} \tag{3}$$

where x_{pi}, y_{pi} and θ_{pi} are translational and angular displacements of the i^{th} phase star-wheel; m_{pi} and j_{pzi} denote the mass and the moment of inertia of the i^{th} phase star-wheel; r_{bp} is the radius of the base circle.

2.1.4 Motion equation of the output shaft subsystem

The output shaft subsystem is composed of the ring gear, the flange, and the output shaft. The ring gear is connected with the flange by bolts, while the flange is connected with the output shaft through a spline. Its corresponding force diagram is shown in Fig. 5.

For convenience, an output shaft coordinate system $O_{o\text{-}xyz}$ is set at the mass center of the output shaft O_o. Herein, the parameters c_1 and c_2 correspond to the distances of the front and the rear bearings on the output shaft from the origin of coordinates to the bearing centers, respectively; c_3 is the distance from O_o to the rear bearing of the input shaft; the parameters c_4 and c_5 correspond to the distances from the coordinate origin to the gear centers of the 1st phase and the 2nd phase star-wheels respectively; g_o is the weight of the

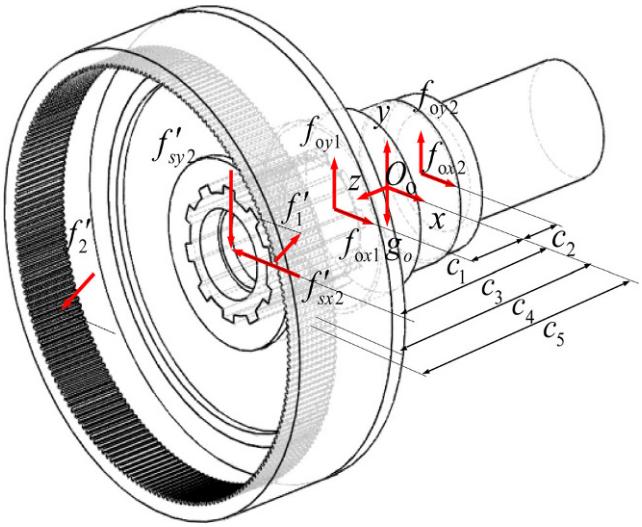

Fig. 5 Force diagram of the output shaft subsystem

output shaft; $f_{ox1}, f_{oy1}, f_{ox2}, f_{oy2}$, f'_{sx2} and f'_{sy2} are the reaction forces of bearings in x and y directions, respectively; f'_1 and f'_2 are the meshing forces between the ring gear and the star-wheel of the 1st phase and the 2nd phase.

The motion equation of the output shaft subsystem can be formulated as

$$\begin{cases} m_o\ddot{x}_o = (f_{ox1} + f'_{x1}) + (f_{ox2} + f'_{x2}) - f'_{sx2} \\ m_o\ddot{y}_o = (f_{oy1} + f'_{y1}) + (f_{oy2} + f'_{y2}) - f'_{sy2} - g_o \\ j_{ox}\ddot{\beta}_{ox} = (-f_{oy1}c_1 - f'_{y1}c_4) + (f_{oy2}c_2 - f'_{y2}c_5) + f'_{sy2}c_3 \\ j_{oy}\ddot{\beta}_{oy} = (f_{ox1}c_1 + f'_{x1}c_4) + (-f_{ox2}c_2 + f'_{x2}c_5)] - f'_{sx2}c_3 \\ j_{oz}\ddot{\beta}_{oz} = f'_1 r_b + f'_2 r_b - T_o \end{cases} \tag{4}$$

where m_o is the mass of the output shaft; j_{ox}, j_{oy} and j_{oz} are the moments of inertia of the output shaft around x, y and z axes, respectively; f'_{xi} and f'_{yi} are the components of meshing force f'_i along x and y directions ($i = 1, 2$); r_b is the base radius of the ring gear; x_o and y_o are the displacements of the output shaft; β_{ox}, β_{oy} and β_{oz} are the angular displacements of the output shaft subsystem.

2.2 Compatible conditions among elastic deformations

Fig. 6 demonstrates the elastic deformation of the i^{th} phase star-wheel, in which the dotted line represents the actual position of the mechanism while the solid line is the theoretical position without elastic deformations and errors.

As shown in Fig. 6, O_IA and O'_IA_2 are the theoretical position and the actual position of the eccentric sleeve on the input shaft; $O_IO'_I$ is the displacement of the input shaft at the i^{th} phase star-wheel; O'_IA_1 and A_1A_2 are the radial and the tangential errors of the eccentric sleeve; A_2A_3 and B_2B_3

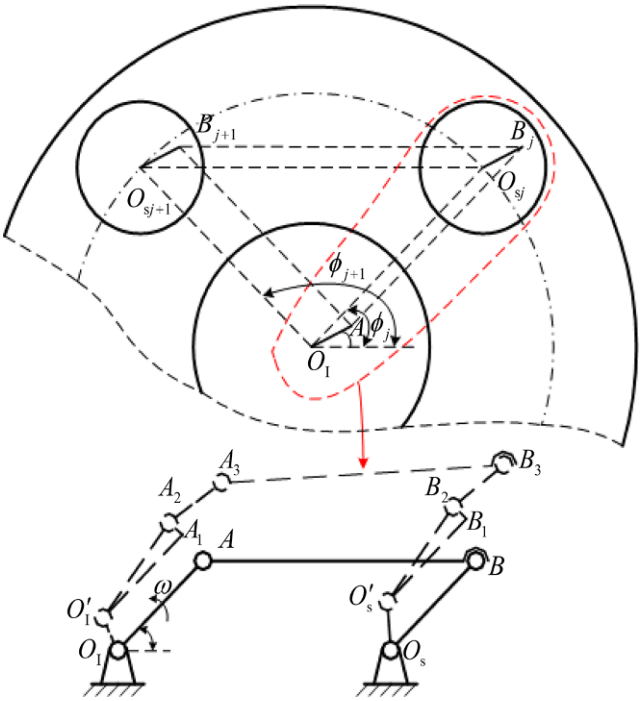

Fig. 6 The elastic deformation of the i^{th} phase star-wheel

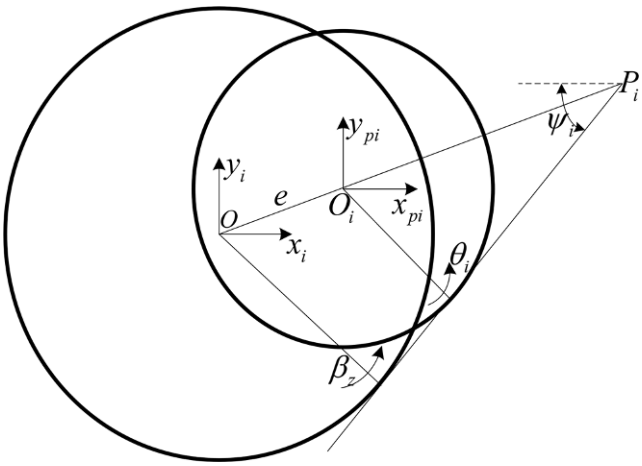

Fig. 7 Deformations between the star-wheel and the ring gear

are the displacements of the star-wheel; O_sB and O'_sB_2 are the theoretical and actual positions of the eccentric sleeve at the star-wheel shaft; O'_sB_1 and B_1B_2 are the radial and the tangential errors of the eccentric sleeve; $O_sO'_s$ is the displacement of the star-wheel shaft at the i^{th} phase position.

According to Fig. 6, the compatible conditions between the input shaft and the i^{th} phase star-wheel can be formulated as

$$u_{ai} = \begin{bmatrix} 1 & 0 & 0 & -a_{i+2} \\ 0 & 1 & a_{i+2} & 0 \end{bmatrix} x_{\mathrm{I}} - \begin{bmatrix} 1 & 0 & 0 \\ 0 & 1 & 0 \end{bmatrix} x_{\mathrm{p}i} + G_i + H_i \tag{5}$$

where $\boldsymbol{u}_{ai}$ is the elastic deformation between the bearing hole of the i^{th} phase star-wheel and the input shaft; $\boldsymbol{x}_{\mathrm{I}}$ and $\boldsymbol{x}_{\mathrm{p}i}$ are the displacement vectors of the input shaft and the i^{th} phase star-wheel; $\boldsymbol{x}_{\mathrm{I}}=(x_{\mathrm{I}},\ y_{\mathrm{I}},\ \beta_{\mathrm{Ix}},\ \beta_{\mathrm{Iy}})^{\mathrm{T}}$, $\boldsymbol{x}_{\mathrm{p}i}=(x_{\mathrm{p}i},\ y_{\mathrm{p}i},\ \theta_{\mathrm{p}i})^{\mathrm{T}}$; $G_i = (\Delta e_{\mathrm{I}i}\cos\varphi_i, \Delta e_{\mathrm{I}i}\sin\varphi_i)^T$ and $H_i = (-e\Delta\theta_{\mathrm{I}i}\sin\varphi_i, e\Delta\theta_{\mathrm{I}i}\cos\varphi_i)^T$ are the radial and the tangential errors of the eccentric sleeve on the input shaft respectively, where $\Delta e_{\mathrm{I}i}$ and $\Delta\theta_{\mathrm{I}i}$ are the radial and the tangential eccentricity errors of the eccentric sleeve.

Similarly, the compatible conditions between the star-wheel shaft and the i^{th} phase star-wheel can be formulated as

$$u_{\mathrm{b}ij} = \begin{pmatrix} 1 & 0 & 0 & (-1)^{i+1}b_{i+2} & -e\sin\varphi_i \\ 0 & 1 & -(-1)^{i+1}b_{i+2} & 0 & e\cos\varphi_i \end{pmatrix} x_{\mathrm{s}j} - \begin{pmatrix} 1 & 0 & -L\sin\phi_j \\ 0 & 1 & L\cos\phi_j \end{pmatrix} x_{\mathrm{p}i} + U_{ij} + V_{ij} \tag{6}$$

where $\boldsymbol{u}_{\mathrm{b}ij}$ is the elastic deformation of the bearing on the star-wheel shaft; $\boldsymbol{x}_{sj}=(x_{sj},\ y_{sj},\ \beta_{sxj},\ \beta_{syj},\ \beta_{szj})^{\mathrm{T}}$ is the displacement vector of the j^{th} star-wheel shaft; $U_{ij} = \left(\Delta e_{\mathrm{s}ij}\cos\varphi_i, \Delta e_{\mathrm{s}ij}\sin\varphi_i\right)^T$ and $V_{ij} = (-e\Delta\theta_{\mathrm{s}ij}\sin\varphi_i, e\Delta\theta_{\mathrm{s}ij}\cos\varphi_i)^T$ are the radial and the tangential errors of the bearing hole on the j^{th} star-wheel shaft, where Δe_{sij} and $\Delta\theta_{sij}$ are radial and tangential error at the bore of the star-wheel bearing.

The following will derive the compatible conditions between the internal gear pairs. Taking the gear meshing of the i^{th} phase star-wheel and the ring gear as an example, Fig. 7 shows the deformation relationship between the two gears.

According to the geometric relationships, the compatibile condition can be formulated as

$$\delta_i = (\sin\psi_i, \cos\psi_i, r_{\mathrm{bp}})x_{\mathrm{p}i} - (\sin\psi_i, \cos\psi_i, -c_{i+3}\cos\psi_i, c_{i+3}\sin\psi_i, r_{\mathrm{b}})x_{\mathrm{o}} \tag{7}$$

where δ_i is the relative displacement along the line of action between the star-wheel and the ring gear; $\boldsymbol{x}_{\mathrm{o}}=(x_{\mathrm{o}},\ y_{\mathrm{o}},\ \beta_{\mathrm{ox}},\ \beta_{\mathrm{oy}},\ \beta_{\mathrm{oz}})^{\mathrm{T}}$ is the displacement vector of the output shaft.

2.3 Governing equations

Substituting Eq. 5 ~ Eq. 7 into Eq. 1 ~ Eq. 4, the elasto-dynamic equation of the transmission system is given as

$$\boldsymbol{M}\ddot{\boldsymbol{X}} + \boldsymbol{K}\boldsymbol{X} = \boldsymbol{F} \tag{8}$$

where $\boldsymbol{X}$ is the displacement vector; $\boldsymbol{M}$ and $\boldsymbol{K}$ denote the mass and the stiffness matrices; and $\boldsymbol{F}$ is the load vector. The details of each matrix can be referred to the appendix.

3 Dynamic analysis

3.1 Example system

Based on the above elasto-dynamic model, an HJW-18B reducer with four star-wheel shafts is taken as an example to illustrate the investigation on the dynamic behaviors of star-wheel reducer. The basic design parameters of the example system are listed in Table 1.

3.2 Modal analysis

The free vibration of the star-wheel reducer can be obtained by ignoring the external load in Eq. 8, which can be written as

$$\boldsymbol{M}\ddot{\boldsymbol{X}} + \boldsymbol{K}\boldsymbol{X} = \boldsymbol{0} \tag{9}$$

The general solution to Eq. 9 can be assumed to be,

$$\boldsymbol{X} = \boldsymbol{\phi}\sin(\omega t + \varphi) \tag{10}$$

where $\boldsymbol{\phi}$ denotes the amplitude of a generalized coordinate; ω denotes the modal frequency of the system; φ denotes the phase of a generalized coordinate. Substitute Eq. 10 into Eq. 9 to obtain the solution expression of system eigenvalues,

$$(\boldsymbol{K} - \omega^2\boldsymbol{M})\boldsymbol{\phi} = \boldsymbol{0} \tag{11}$$

The modal characteristic of the system can be obtained by solving Eq. 11. Herein, the parameters listed in Table 1 are taken as an example to investigate the modal characteristic of the star-wheel reducer. The first 6 orders modal frequencies and the modal coordinates of the star-wheel are shown in Table 2.

As illustrated in Table 2, the first 6 orders modal frequencies are in the range of 66.2 to 197 Hz. The first order modal frequency is 66.2 Hz, which is much higher than the input frequency of the star-wheel reducer (16.7 Hz under input speed 1000 r/min). Hence, there would be no resonance occurs during work. To further intuitively understand the vibration of each subsystem of the star-wheel, the modal energy distribution of the low-frequency modes are calculated and shown in Fig. 8. Here, 'O' is used to represent the subsystem of the output shaft; 'I' denotes the subsystem of the input shaft; 'S1', 'S2', 'S3' and 'S4' are subsystems of the 1st, the 2nd, the 3rd and the 4th star-wheel shafts; 'P1' and 'P2' denote the subsystems of the two star-wheels.

By observing the modal coordinates listed in Table 2 and the modal energy distribution in Fig. 8, one may find that the modal shapes corresponding to the modal frequency can be described as:

1. $f_1 = 66.2$ Hz. As can be seen from Table 2, the subsystem of the output shaft is in a torsion state; input shaft is in

Table 1 Basic parameters of HJW-18B star-wheel reducer

Parameters	Value	Parameters	Value
Tooth number of star-wheel z_1	192	Modification coefficient of star-wheel x_1	0.01
Tooth number of ring gear z_2	196	Modification coefficient of ring gear x_2	0.1
Modulus m/mm	1.5	Distribution radius of star-wheel shaft L/mm	90
Eccentricity e/mm	3.12	Stiffness of star-wheel shaft bearing $k_s/(N\cdot m^{-1})$	3×10^7
Transmission ratio	50	Stiffness of star-wheel bearing $k_p/(N\cdot m^{-1})$	3×10^7
Rated speed $n/(r\cdot min^{-1})$	1000	Stiffness of input shaft front bearing $k_{I1}/(N\cdot m^{-1})$	1×10^7
Input power P/kW	10	Stiffness of input shaft rear bearing $k_{I2}/(N\cdot m^{-1})$	2×10^7
Angle of engagement $\alpha/(°)$	25	Stiffness of output shaft front bearing $k_{o1}/(N\cdot m^{-1})$	3×10^7
Average mesh stiffness $k_m/(N\cdot m^{-1})$	3×10^8	Stiffness of output shaft rear bearing $k_{o2}/(N\cdot m^{-1})$	4×10^7
Mass of output shaft subsystem m_o/kg	38.5	Mass of star-wheel shaft subsystem m_s/kg	0.515
Moment of inertia $J_{ox}/(kg\cdot m^2)$	0.518	Moment of inertia $J_{sx}/(kg\cdot m^2)$	6.5×10^{-4}
Moment of inertia $J_{oy}/(kg\cdot m^2)$	0.518	Moment of inertia $J_{sy}/(kg\cdot m^2)$	6.5×10^{-4}
Moment of inertia $J_{oz}/(kg\cdot m^2)$	0.36	Moment of inertia $J_{sz}/(kg\cdot m^2)$	5.9×10^{-4}
Mass of input shaft subsystem m_I/kg	5	Mass of star-wheel subsystem m_p/kg	7
Moment of inertia $J_{Ix}/(kg\cdot m^2)$	1.7×10^{-2}	Moment of inertia $J_{pz}/(kg\cdot m^2)$	7.1×10^{-2}
Moment of inertia $J_{Iy}/(kg\cdot m^2)$	1.7×10^{-2}		

Table 2 The first 6 orders modal coordinates

Coordinates		$f_1 = 66.2$ Hz	$f_2 = 102.5$ Hz	$f_3 = 113.5$ Hz	$f_4 = 145.6$ Hz	$f_5 = 145.6$ Hz	$f_6 = 197$ Hz
$\boldsymbol{X}_o$	X_o	–0.0013	0.0011	0.0379	0.0000	0.0000	0.0058
	Y_o	0.0011	–0.0134	0.0033	0.0000	0.0000	–0.0675
	β_{ox}	–0.0053	0.4248	–0.1171	0.0000	0.0000	–1.0532
	β_{oy}	–0.0239	0.0364	1.3405	0.0000	0.0000	–0.0910
	β_{oz}	–0.3439	–0.0520	–0.0079	0.0000	0.0000	0.5970
$\boldsymbol{x}_I$	x_I	0.0021	0.0003	0.0134	0.0000	0.0000	–0.0018
	y_I	–0.0039	–0.0037	0.0011	0.0000	0.0000	0.0229
	β_{Ix}	0.0746	–0.1202	0.0340	0.0000	0.0000	–0.0103
	β_{Iy}	0.0486	–0.0100	–0.3715	0.0000	0.0000	0.0029
$\boldsymbol{x}_{s1}$	x_{s1}	–0.0002	0.0001	0.0068	0.0000	0.0000	–0.0014
	y_{s1}	–0.0007	–0.0020	0.00053	0.0000	0.0000	0.0354
	β_{sx1}	–0.1192	–0.2286	–0.00067	–0.0014	–0.7450	–0.4992
	β_{sy1}	–0.0663	–0.3996	–0.0141	–0.0008	–0.4301	–0.1187
	β_{sz1}	–19.4075	–23.5328	–0.3684	–0.0479	–25.1098	–7.7836
$\boldsymbol{x}_{s2}$	x_{s2}	0.0008	0.0005	0.0069	0.0000	0.0000	–0.0209
	y_{s2}	0.0003	–0.0016	0.0006	0.0000	0.0000	0.0158
	β_{sx2}	–0.1136	–0.4016	–0.0007	0.2589	0.9263	–0.2213
	β_{sy2}	–0.0780	0.2340	–0.0140	0.1495	0.5348	–0.2757
	β_{sz2}	–19.4075	–13.6551	–0.3660	8.7248	31.2205	–5.2168
$\boldsymbol{x}_{s3}$	x_{s3}	0.0002	0.0001	0.0068	0.0000	0.0000	–0.0014
	y_{s3}	0.0013	–0.0013	0.0007	0.0000	0.0000	–0.0037
	β_{sx3}	–0.1182	0.2231	–0.0005	0.7019	–0.2497	0.2659
	β_{sy3}	–0.0767	0.3981	–0.0139	0.4053	–0.1442	0.0906
	β_{sz3}	–20.0147	23.2088	–0.3569	23.6578	–8.4151	4.3625
$\boldsymbol{x}_{s4}$	x_{s4}	–0.0012	–0.0002	0.0067	0.0000	0.0000	0.0182
	y_{s4}	0.0003	–0.0016	0.0006	0.0000	0.0000	0.0158
	β_{sx4}	–0.1239	0.3961	–0.0005	–0.9594	0.0684	–0.012
	β_{sy4}	–0.0650	–0.2355	–0.0141	–0.5539	0.0395	0.2476
	β_{sz4}	–19.8864	13.3311	–0.3594	–32.3346	2.3044	1.7957
$\boldsymbol{x}_{p1}$	x_{p1}	0.0237	0.0005	0.0129	0.0000	0.0000	–0.0014
	y_{p1}	–0.0417	–0.0035	0.0003	0.0000	0.0000	0.0373
	θ_{p1}	–0.0125	–0.4806	–0.0017	0.0000	0.0000	0.6340
$\boldsymbol{x}_{p2}$	x_{p2}	–0.0247	0.0001	0.0143	0.0000	0.0000	–0.0042
	y_{p2}	0.0431	–0.0031	0.0021	0.0000	0.0000	0.0255
	θ_{p2}	–0.0318	0.4639	–0.0015	0.0000	0.0000	0.2292

an oscillation state; star-wheel shaft is in a torsion state and star-wheel is in an inactive state. It can be seen from Fig. 8 that the oscillation of the input shaft dominates the modal energy.

2. $f_2 = 102.5$ Hz. Both the subsystems of the output shaft and the input shaft are in the state of oscillation; and the subsystems of the star-wheel shaft and the star-wheel are in the state of torsion. It can be seen that the oscillation of the output shaft dominates the modal energy.
3. $f_3 = 113.5$ Hz. Both the subsystems of the output shaft and the input shaft are in the state of oscillation; the star-wheel shaft is in a torsion state and the star-wheel is in an inactive state. It can be seen that the oscillation of the subsystem of output shaft dominates the modal energy.
4. $f_4 = f_5 = 145.6$ Hz. Different from the first 3 orders natural frequencies, the 4th and the 5th natural frequencies are the same. The subsystems of the input shaft, the output shaft and the star-wheel are all inactivity. Only the star-wheel shaft has torsion and oscillation motions.
5. $f_6 = 197$ Hz. The subsystems of the output shaft and the star-wheel shaft are in the coupling state of oscillation and torsion; the input shaft is in an inactive state and the star-wheel is in a torsion state. The coupling motion state of the output shaft subsystem is the most overwhelming modal shape.

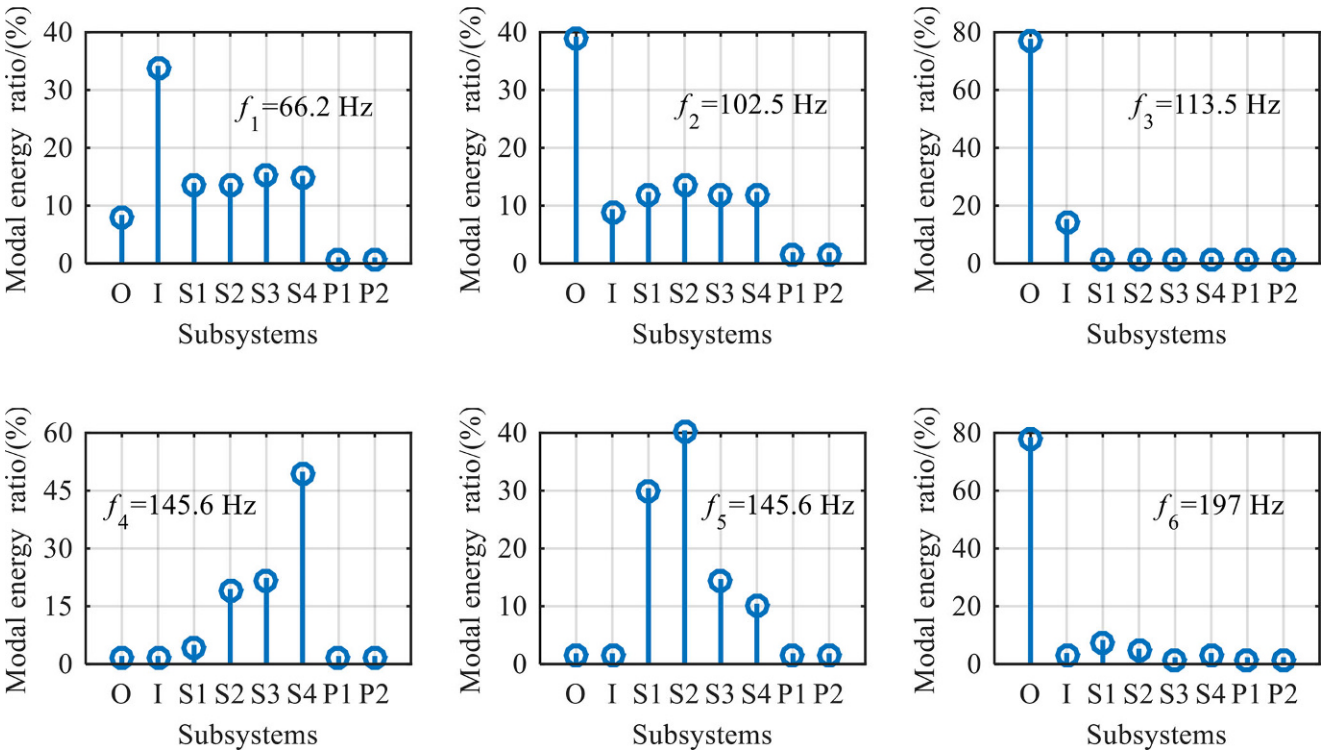

Fig. 8 The modal energy distribution of the first 6 orders

3.3 Dynamic responses

In addition to the modal characteristics, the force of each component is also concerned. For simplicity, the following settings are assumed: 1) all the manufacturing errors in the dynamic model are set to be zero; 2) the meshing stiffness of internal gear pairs is set as the average value of meshing stiffness.

Based on the above assumptions, the dynamic meshing forces, the dynamic forces of the star-wheel bearings and the dynamic forces of the star-wheel shaft bearings are calculated and depicted in Fig. 9.

As shown in Fig. 9(a), the dynamic meshing forces of the two meshing pairs are symmetric with small fluctuation. The dynamic meshing force of the 1st phase star-wheel decrease firstly and then increase gradually while the dynamic meshing force of the 2nd phase is opposite due to the load balance. For instance, the maximum dynamic meshing forces of the 1st phase and the 2nd phase star-wheel pair are 3790 and 3526 N while the minimum values are 3716 and 3451 N. The fluctuation amplitudes of the dynamic meshing forces are only 74 and 75 N respectively. Further analysis shows that the sum of the two phase dynamic meshing forces is 7241 N approximately at any time. All the above data shows the stability of the star-wheel reducer.

Fig. 9(b) shows the variation of the dynamic forces of the star-wheel bearings. It can be seen that the dynamic force of the 1st phase star-wheel bearing increases first and then decreases, while the trend of the dynamic force on the 2nd phase is opposite. To be more specific, the mean value of the dynamic force of the 1st phase star-wheel bearing is larger than that of the 2nd phase, which is potentially related to the dynamic meshing force of different star-wheels. However, the amplitude fluctuation of the dynamic forces of different star-wheel bearings is the same, which is only 63 N.

Fig. 9(c) and Fig. 9(d) show the dynamic forces of star-wheel shaft bearings on the 1st phase and the 2nd phase star-wheel. Herein, the 1st phase star-wheel is taken as an example to illustrate the dynamic force of the bearings on four star-wheel shafts. It can be found that the dynamic forces of four star-wheel shaft bearings are different in value and phase. But the fluctuation trend of the dynamic bearing forces on four star-wheel shafts are similar but with a phase difference of 90°. The mean dynamic force of the first, the second, the third and the fourth star-wheel shaft bearing are 1445 N, 1416 N, 1385 N and 1415 N, respectively. From this data, it can be seen that the difference of the dynamic force of four star-wheel bearings is small. What's more, the sum of the bearing dynamic forces of the 1st and the 3rd star-wheel shaft is equal to that of the 2nd and the 4th star-wheel shaft. This data shows that the star-wheel bearing can bear the load evenly and can avoid the premature failure.

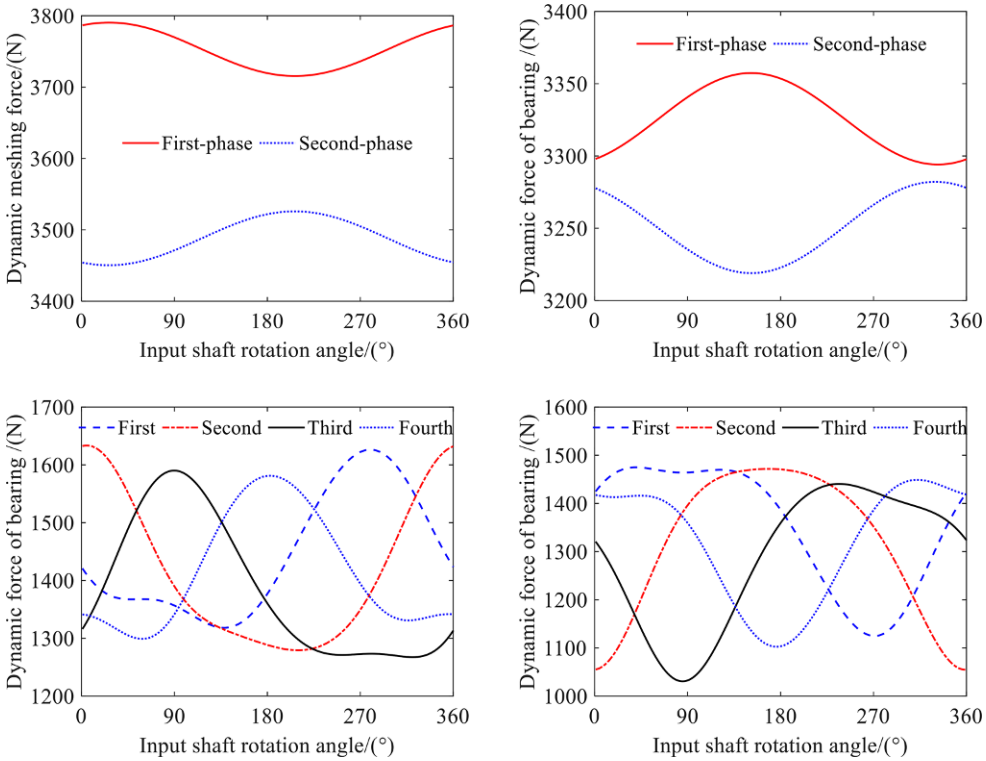

Fig. 9 Dynamic forces of the star-wheel reducer components: (**a**) gears (**b**) the star-wheel bearings (**c**) bearings on the 1st phase star-wheel shafts (**d**) bearings on the 2nd phase star-wheel shafts

4 Experimental validations

In order to verify the modeling and dynamic analysis, a modal test and a vibration test are carried out in this section.

4.1 Modal test

The modal test is used to verify the correctness of the modeling and modal solution. The impact method is adopted in the test. The schematic diagram and experimental scene are shown in Fig. 10.

The frequency response functions are shown in the Fig. 11. Herein, blue and red lines are the frequency response function of the input and the output signals in x axis direction, respectively. The comparison of the modal experiment and the theoretical calculation are shown in the Table 3.

As can be seen in Table 3, the lower orders modal frequencies obtained from the theoretical elasto-dynamic model and the experimental test are relatively close despite the calculation error of the third order modal frequency between the theoretical and experimental results is 17%. In general, the results of the theoretical calculation agree well with the measured results from modal experiment, indicating the correctness of the theoretical analysis. Therefore, the presented elasto-dynamic model can be applied for further studies, such as dynamic analysis and parameter optimization.

Table 3 Comparison between the theoretical results and the tested results

Modes	Theoretical calculation/Hz	Experimental modal/Hz	Error/%
1	66.2	62.1	6.19
2	102.5	96.6	5.76
3	113.5	132.8	17.00
4	145.6	156.3	7.35
5	197	192.2	2.44
6	214	231.3	8.08

4.2 Vibration test

A back-to-back star-wheel reducer test rig is set up to investigate the vibration characteristics of the system. The layout of test rig and the acceleration sensors are shown in Fig. 12.

Based on the arrangement, the vibration acceleration of the input shaft and the output shaft of the star-wheel reducer are collected. The vibration signals in both time domain and frequency domain are demonstrated as follows.

As can be seen in Fig. 13 and 14, the frequencies corresponding to the spectrum peak are 332 Hz, 490 Hz, 580 Hz, 654 Hz, 736 Hz, 818 Hz, 896 Hz, 978 Hz, respectively. The input rotational frequency, meshing frequency are 16.7 and 3200 Hz can be obtained from the prototype parameters

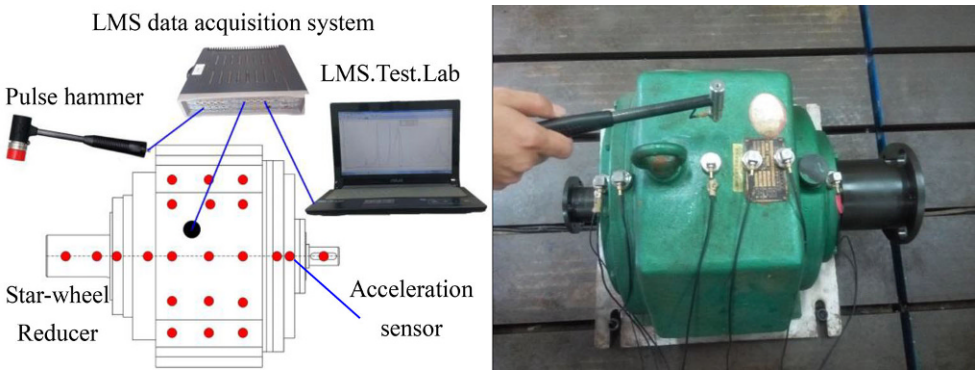

Fig. 10 Schematic diagram and experimental scene

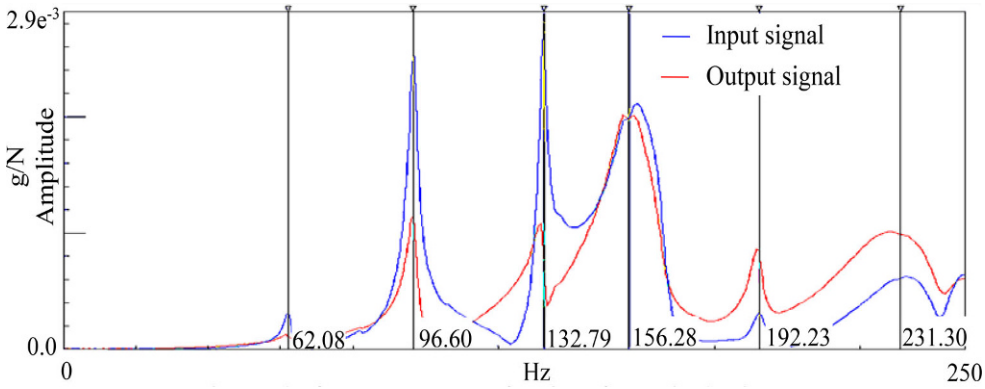

Fig. 11 The frequency response function of star-wheel reducer

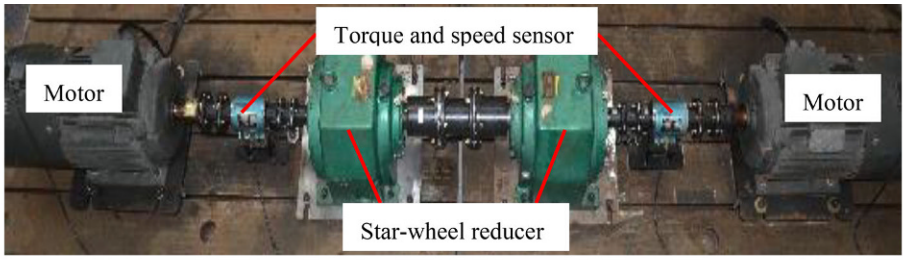

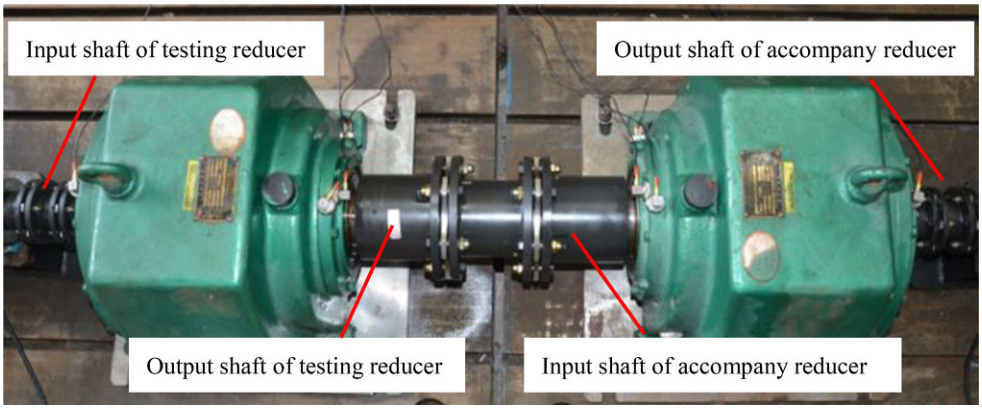

Fig. 12 Test rig and acceleration sensors

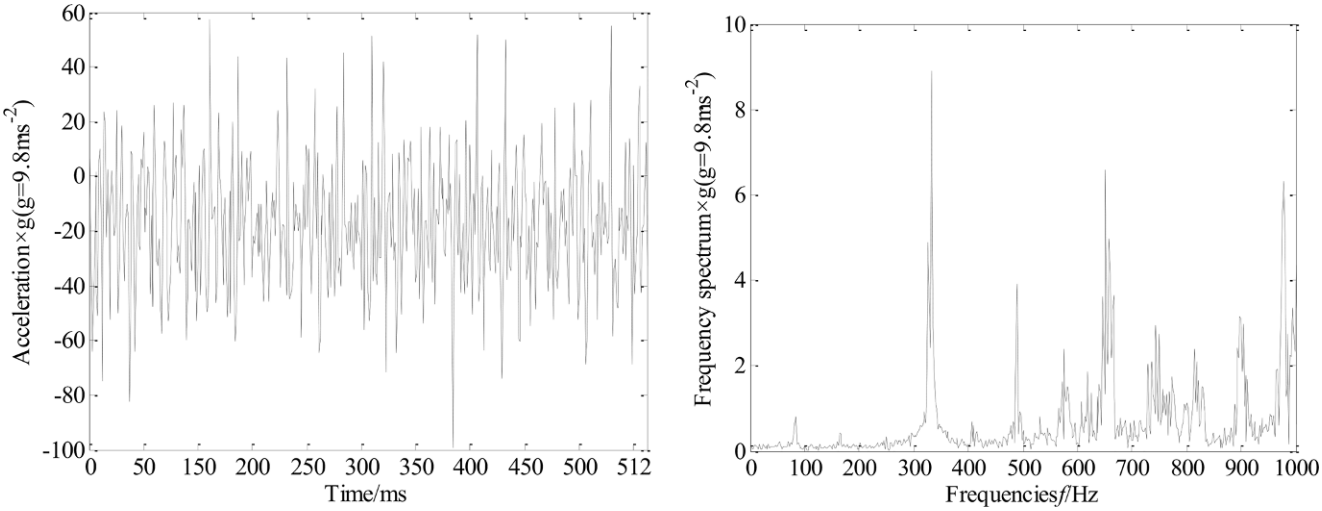

Fig. 13 Time domain waveform and frequency spectrum of the input shaft

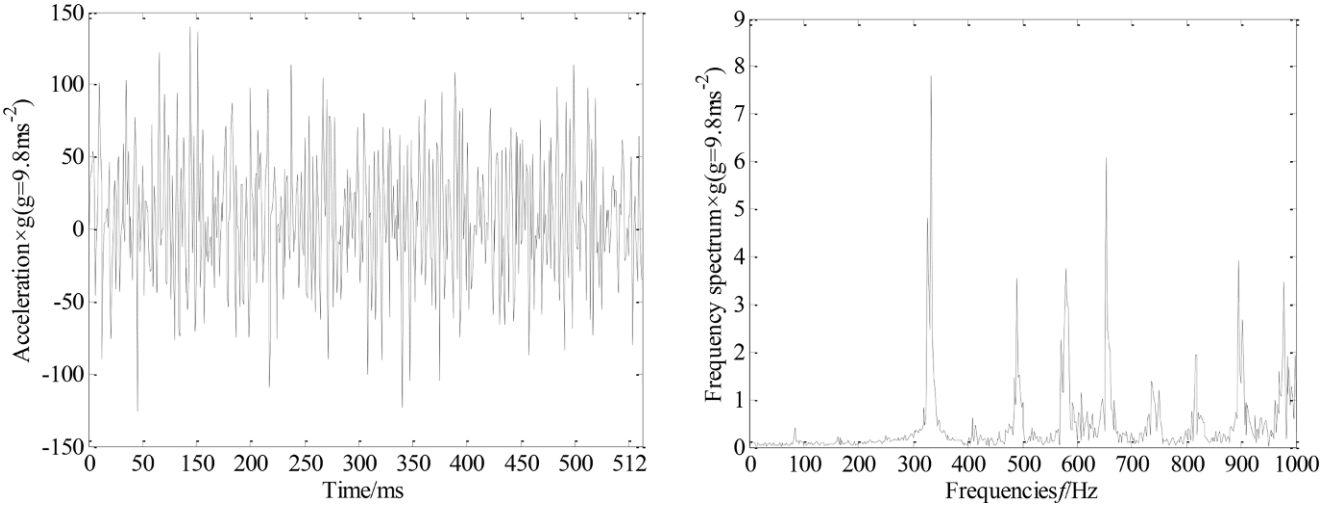

Fig. 14 Time domain waveform and frequency spectrum of the output shaft

($n = 1000$ r/min). It can be seen that the vibration of the system is not caused by the excitation of the input shaft, because the frequency of rotation is far less than the resonance frequency.

The frequencies corresponding to the first three large amplitudes are 332 Hz, 654 Hz and 978 Hz, which are approximate to 5, 10 and 15 times of the modal frequency ($f_1 = 66.2$ Hz); 490 Hz and 736 Hz are approximate to 1/3 and 1/2 of the 4th modal frequency of the star-wheel reducer box ($f_{b4} = 1452$ Hz); 580 Hz is 4 times of the 4th modal frequency ($f_4 = 145.6$ Hz) and 818 Hz is 3 times of the 8th modal frequency ($f_8 = 272.5$ Hz); The 896 Hz is not close to the multiple frequencies of the first 8 orders modal frequencies, and it may be caused by the superposition of several modal frequencies.

5 Conclusions

1. An elasto-dynamic model of the star-wheel reducer is established by substructure synthesis method, whose correctness and accuracy is verified by a modal test and a vibration test.
2. There is no structural resonance in the star-wheel reducer because the low-order modal frequency of the system is much higher than the input rotational frequency. However, the low-order mode of the system is complex, which is generally manifested as the coupling of torsion and swing of several components.
3. The dynamic meshing forces of the star-wheel gear pairs are not evenly distributed, but the fluctuation amplitude of the two-phase star-wheels are very small and their

fluctuation trends are similar with only a phase difference of 180°.

4. The fluctuation trends of the dynamic forces of star-wheel bearings are similar with a phase difference of 90°. The variation trends of the dynamic forces of bearings on different star-wheels are opposite to each other.

6 Comment on the future work

In the present study, an elasto-dynamic model of star-wheel reducer is established, based on which the modal characteristics as well steady dynamic responses are theoretically investigated and experimentally validated. Based on the dynamic model and analysis, the effects of manufacturing errors and shafts misalignments on the dynamic responses will be studied in our future work.

Acknowledgements This work was sponsored by National Natural Science Foundation of China (Grant No. 51875105).

Appendix

The elements of the mass, stiffness, load and displacement matrix in Eq. 8 are as follows,

$$\boldsymbol{M} = \begin{bmatrix} m_{\mathrm{o}} & & & \\ & m_{\mathrm{I}} & & \\ & & m_{\mathrm{s}j} & \\ \mathrm{sym} & & & m_{\mathrm{p}i} \end{bmatrix},$$

$$\boldsymbol{K} = \begin{bmatrix} k_{\mathrm{o}} & k_{\mathrm{o,I}} & & k_{\mathrm{o,p}i} \\ & k_{\mathrm{I}} & & k_{\mathrm{I,p}i} \\ & & k_{\mathrm{s}j} & k_{\mathrm{s,p}i} \\ \mathrm{sym} & & & k_{\mathrm{p}i} \end{bmatrix}, \boldsymbol{F} = \begin{bmatrix} f_{\mathrm{o}} \\ f_{\mathrm{I}} \\ f_{\mathrm{s}j} \\ f_{\mathrm{p}i} \end{bmatrix}, \boldsymbol{X} = \begin{bmatrix} x_{\mathrm{o}} \\ x_{\mathrm{I}} \\ x_{\mathrm{s}j} \\ x_{\mathrm{p}i} \end{bmatrix}$$

Further, ***M, K, F*** and ***X*** matrix are composed of the parameters of each subsystem, as shown below:

Output shaft subsystem

$$m_{\mathrm{o}} = \begin{bmatrix} m_{\mathrm{o}} & & & & \\ & m_{\mathrm{o}} & & & \\ & & j_{\mathrm{o}x} & & \\ & & & j_{\mathrm{o}y} & \\ \mathrm{sym} & & & & j_{\mathrm{o}z} \end{bmatrix}, \; x_{\mathrm{o}} = \begin{bmatrix} x_{\mathrm{o}} \\ y_{\mathrm{o}} \\ \beta_{\mathrm{o}x} \\ \beta_{\mathrm{o}y} \\ \beta_{\mathrm{o}z} \end{bmatrix},$$

$$f_{\mathrm{o}} = \begin{bmatrix} 0 \\ -g_{\mathrm{o}} \\ 0 \\ 0 \\ -T_{\mathrm{o}} \end{bmatrix}, \; k_{\mathrm{oI}} = k_{\mathrm{I2}} \begin{bmatrix} -1 & & & a_2 \\ & -1 & -a_2 & 0 \\ & c_3 & a_2 c_3 & 0 \\ -c_3 & & & a_2 c_3 \\ 0 & 0 & 0 & 0 \end{bmatrix},$$

$$k_{\mathrm{op}i} = -k_{\mathrm{m}} \sum_{i=1}^{2} \begin{bmatrix} \sin^2\psi_i & \sin\psi_i\cos\psi_i & r_{\mathrm{bp}}\sin\psi_i \\ \sin\psi_i\cos\psi_i & \cos^2\psi_i & r_{\mathrm{bp}}\cos\psi_i \\ -c_{i+3}\sin\psi_i\cos\psi_i & -c_{i+3}\cos^2\psi_i & -c_{i+3}r_{\mathrm{bp}}\cos\psi_i \\ c_{i+3}\sin^2\psi_i & c_{i+3}\sin\psi_i\cos\psi_i & c_{i+3}r_{\mathrm{bp}}\sin\psi_i \\ r_b\sin\psi_i & r_b\cos\psi_i & r_b r_{\mathrm{bp}} \end{bmatrix},$$

$$k_{\mathrm{o}} = k_{\mathrm{o}}^1 + k_{\mathrm{o}}^2 + k_{\mathrm{o}}^3,$$

$$k_{\mathrm{o}}^1 = \sum_{i=1}^{2} \begin{bmatrix} k_{\mathrm{o}i} & 0 & 0 & (-1)^{i+1}k_{\mathrm{o}i}c_i & 0 \\ & k_{\mathrm{o}i} & -(-1)^{i+1}k_{\mathrm{o}i}c_i & 0 & 0 \\ & & k_{\mathrm{o}i}c_i^2 & 0 & 0 \\ & & & k_{\mathrm{o}i}c_i^2 & 0 \\ \mathrm{sym} & & & & 0 \end{bmatrix},$$

$$k_{\mathrm{o}}^2 = k_{\mathrm{I2}} \begin{bmatrix} 1 & 0 & 0 & c_3 & 0 \\ & 1 & -c_3 & 0 & 0 \\ & & c_3^2 & 0 & 0 \\ & & & c_3^2 & 0 \\ \mathrm{sym} & & & & 0 \end{bmatrix},$$

$$k_{\mathrm{o}}^3 = k_{\mathrm{m}} \sum_{i=1}^{2} \begin{bmatrix} \sin^2\psi_i & \sin\psi_i\cos\psi_i & -c_{i+3}\sin\psi_i\cos\psi_i & c_{i+3}\sin^2\psi_i & r_{\mathrm{b}}\sin\psi_i \\ \sin\psi_i\cos\psi_i & \cos^2\psi_i & -c_{i+3}\cos^2\psi_i & c_{i+3}\sin\psi_i\cos\psi_i & r_{\mathrm{b}}\cos\psi_i \\ -c_{i+3}\sin\psi_i\cos\psi_i & -c_{i+3}\cos^2\psi_i & c_{i+3}^2\cos^2\psi_i & -c_{i+3}^2\sin\psi_i\cos\psi_i & -c_{i+3}r_{\mathrm{b}}\cos\psi_i \\ c_{i+3}\sin^2\psi_i & c_{i+3}\sin\psi_i\cos\psi_i & -c_{i+3}^2\sin\psi_i\cos\psi_i & c_{i+3}^2\sin^2\psi_i & c_{i+3}r_{\mathrm{b}}\sin\psi_i \\ r_b\sin\psi_i & r_b\cos\psi_i & -c_{i+3}r_{\mathrm{b}}\cos\psi_i & c_{i+3}r_{\mathrm{b}}\sin\psi_i & r_b^2 \end{bmatrix}$$

Input shaft subsystem

$$m_{\mathrm{I}} = \begin{bmatrix} m_{\mathrm{I}} & & & \\ & m_{\mathrm{I}} & & \\ & & j_{\mathrm{I}x} & \\ \mathrm{sym} & & & j_{\mathrm{I}y} \end{bmatrix},\ x_{\mathrm{I}} = \begin{bmatrix} x_{\mathrm{I}} \\ y_{\mathrm{I}} \\ \beta_{\mathrm{I}x} \\ \beta_{\mathrm{I}y} \end{bmatrix},\ f_{\mathrm{I}} = f_{\mathrm{I}1} + f_{\mathrm{I}2},$$

$$f_{\mathrm{I}1} = \begin{bmatrix} 0 \\ -g_{\mathrm{I}} \\ m_{e1} e\omega^2 \sin\varphi_1\ (a_3 + a_4) \\ -m_{e1} e\omega^2 \cos\varphi_1\ (a_3 + a_4) \end{bmatrix},$$

$$f_{\mathrm{I}2} = -k_{\mathrm{a}} \sum_{i=1}^{2} \begin{bmatrix} 1 & 0 \\ 0 & 1 \\ 0 & a_{i+2} \\ -a_{i+2} & 0 \end{bmatrix} (G_i + H_i),$$

$$k_{\mathrm{Io}} = k_{\mathrm{I}2} \begin{bmatrix} -1 & 0 & 0 & -c_3 & 0 \\ 0 & -1 & c_3 & 0 & 0 \\ 0 & -a_2 & c_3 a_2 & 0 & 0 \\ a_2 & 0 & 0 & c_3 a_2 & 0 \end{bmatrix} = (k_{\mathrm{oI}})^{\mathrm{T}},$$

$$k_{\mathrm{I}} = \begin{bmatrix} 2 + \sum k_{\mathrm{I}i} & 0 & 0 & \sum (-1)^{i+1} k_{\mathrm{I}i} a_i - \sum k_{\mathrm{a}} a_{i+2} \\ & 2 + \sum k_{\mathrm{I}i} & \sum k_{\mathrm{a}} a_{i+2} - \sum (-1)^{i+1} k_{\mathrm{I}i} a_i & \\ & & \sum k_{\mathrm{a}} a_{i+2}^2 + \sum k_{\mathrm{I}i} a_i^2 & \\ \mathrm{sym} & & & \sum k_{\mathrm{a}} a_{i+2}^2 + \sum k_{\mathrm{I}i} a_i^2 \end{bmatrix}, i = 1,2,$$

$$k_{\mathrm{I}pi} = -k_{\mathrm{a}} \begin{bmatrix} 1 & & 0 \\ & 1 & 0 \\ & a_{i+2} & 0 \\ -a_{i+2} & & 0 \end{bmatrix} = (k_{\mathrm{p}Ii})^{\mathrm{T}}$$

Star-wheel shaft subsystem

$$m_{sj} = \begin{bmatrix} m_{sj} & & & & \\ & m_{sj} & & & \\ & & j_{sxj} & & \\ & & & j_{syj} & \\ \text{sym} & & & & j_{szj} \end{bmatrix},$$

$$x_{sj} = \begin{bmatrix} x_{sj} \\ y_{sj} \\ \beta_{sxj} \\ \beta_{syj} \\ \beta_{szj} \end{bmatrix},\ f_{sj} = f_{sj1} + f_{sj2},$$

$$f_{sj1} = \begin{bmatrix} 0 \\ -g_s \\ -m_{es} e\omega^2 \sin\varphi_1 \,(b_3 + b_4) \\ m_{es} e\omega^2 \cos\varphi_1 \,(b_3 + b_4) \\ 0 \end{bmatrix},$$

$$f_{sj2} = -k_p \sum_{i=1}^{2} \begin{bmatrix} 1 & & \\ & 1 & \\ & -b_{i+2} & \\ b_{i+2} & & \\ -e\sin\varphi_i & e\cos\varphi_i & \end{bmatrix} \left(U_{ij} + V_{ij}\right),$$

$$k_{spi} = -k_p \begin{bmatrix} 1 & & -L\sin\phi_j \\ & 1 & L\cos\phi_j \\ & -b_{i+2} & -b_{i+2} L\cos\phi_j \\ b_{i+2} & & -b_{i+2} L\sin\phi_j \\ -e\sin\varphi_i & e\cos\varphi_i & eL\sin\varphi_i \sin\phi_j + eL\cos\varphi_i \cos\phi_j \end{bmatrix} = (k_{psi})^{\mathrm{T}},$$

$$k_s = \sum_{i=1}^{2} \begin{bmatrix} k_{si} & & & (-1)^{i+1} k_{si} b_i \\ & k_{si} & -(-1)^{i+1} k_{si} b_i & \\ & & k_{si} b_i^2 & \\ & & & k_{si} b_i^2 \\ \text{sym} & & & 0 \end{bmatrix}$$

$$+ k_p \sum_{i=1}^{2} \begin{bmatrix} 1 & & & b_{i+2} & -e\sin\varphi_i \\ & 1 & -b_{i+2} & & e\cos\varphi_i \\ & -b_{i+2} & b_{i+2}^2 & & -b_{i+2} e\cos\varphi_i \\ b_{i+2} & & & b_{i+2}^2 & -b_{i+2} e\sin\varphi_i \\ -e\sin\varphi_i & e\cos\varphi_i & -b_{i+2} e\cos\varphi_i & -b_{i+2} e\sin\varphi_i & e^2 \end{bmatrix}$$

The i^{th} phase star-wheel subsystem

$$m_{\mathrm{p}i} = \begin{bmatrix} m_{\mathrm{p}i} & & \\ & m_{\mathrm{p}i} & \\ \mathrm{sym} & & j_{\mathrm{p}zi} \end{bmatrix},\ f_{\mathrm{p}i1} = \begin{bmatrix} 0 \\ -g_{\mathrm{p}} \\ 0 \end{bmatrix},$$

$$f_{\mathrm{p}i2} = \begin{bmatrix} m_{\mathrm{p}} e\omega^2 \cos\varphi_i \\ m_{\mathrm{p}} e\omega^2 \sin\varphi_i \\ 0 \end{bmatrix},$$

$$f_{\mathrm{p}i3} = k_{\mathrm{a}} \begin{bmatrix} 1 & 0 \\ 0 & 1 \\ 0 & 0 \end{bmatrix} (G_i + H_i)$$

$$f_{\mathrm{p}i4} = k_{\mathrm{p}} \sum_{j=1}^{m} \begin{bmatrix} 1 & 0 \\ 0 & 1 \\ -L\sin\phi_j & L\cos\phi_j \end{bmatrix} \left(U_{ij} + V_{ij}\right),$$

$$x_{\mathrm{p}i} = \begin{bmatrix} x_{\mathrm{p}i} \\ y_{\mathrm{p}i} \\ \theta_{\mathrm{p}i} \end{bmatrix},$$

$$k_{\mathrm{pI}i} = -k_{\mathrm{a}} \begin{bmatrix} 1 & 0 & 0 & -a_{i+2} \\ 0 & 1 & a_{i+2} & 0 \\ 0 & 0 & 0 & 0 \end{bmatrix} k_{\mathrm{p}i}^1 = k_{\mathrm{m}} \begin{bmatrix} \sin^2\psi_i & \sin\psi_i\cos\psi_i & r_{\mathrm{bp}}\sin\psi_i \\ \sin\psi_i\cos\psi_i & \cos^2\psi_i & r_{\mathrm{bp}}\cos\psi_i \\ r_{\mathrm{bp}}\sin\psi_i & r_{\mathrm{bp}}\cos\psi_i & r_{\mathrm{bp}}^2 \end{bmatrix},$$

$$k_{\mathrm{p}i}^2 = k_{\mathrm{p}} \begin{bmatrix} m & 0 & 0 \\ 0 & m & 0 \\ 0 & 0 & mL^2 \end{bmatrix},\ k_{\mathrm{p}i}^3 = k_{\mathrm{a}} \begin{bmatrix} 1 & 0 & 0 \\ 0 & 1 & 0 \\ 0 & 0 & 0 \end{bmatrix},$$

$$k_{\mathrm{po}i} = -k_{\mathrm{m}} \begin{bmatrix} \sin^2\psi_i & \sin\psi_i\cos\psi_i & -c_{i+3}\sin\psi_i\cos\psi_i & c_{4,5}\sin^2\psi_i & r_{\mathrm{b}}\sin\psi_i \\ \sin\psi_i\cos\psi_i & \cos^2\psi_i & -c_{i+3}\cos^2\psi_i & c_{i+3}\sin\psi_i\cos\psi_i & r_{\mathrm{b}}\cos\psi_i \\ r_{\mathrm{bp}}\sin\psi_i & r_{\mathrm{bp}}\cos\psi_i & -c_{i+3}r_{\mathrm{bp}}\cos\psi_i & c_{4,5}r_{\mathrm{bp}}\sin\psi_i & r_{\mathrm{bp}}r_{\mathrm{b}} \end{bmatrix}$$

$$k_{\mathrm{ps}ij} = -k_{\mathrm{p}} \sum_{j=1}^{m} \begin{bmatrix} 1 & 0 & 0 & b_{i+2} & -e\sin\varphi_i \\ 0 & 1 & -b_{i+2} & 0 & e\cos\varphi_i \\ -L\sin\phi_j & L\cos\phi_j & -L\cos\phi_j b_{i+2} & -L\sin\phi_j b_{i+2} & eL\cos\varphi_i\cos\phi_j + eL\sin\varphi_i\sin\phi_j \end{bmatrix} x_{\mathrm{s}j},$$

$$k_{\mathrm{p}i} = k_{\mathrm{p}i}^1 + k_{\mathrm{p}i}^2 + k_{\mathrm{p}i}^3,$$

$$f_{\mathrm{p}i} = f_{\mathrm{p}i1} + f_{\mathrm{p}i2} + f_{\mathrm{p}i3} + f_{\mathrm{p}i4}$$

References

1. Liang X, Zuo MJ, Feng Z (2018) Dynamic modeling of gearbox faults: a review. Mech Syst Signal Process 98:852–876
2. Liu X, Yang Y, Zhang J (2018) Resultant vibration signal model based fault diagnosis of a single stage planetary gear train with an incipient tooth crack on the sun gear. Renew Energy 122:65–79
3. Yi Y, Qin D, Liu C (2018) Investigation of electromechanical coupling vibration characteristics of an electric drive multistage gear system. Mech Mach Theory 121:446–459
4. Leque N, Kahraman A (2017) A three-dimensional load sharing model of planetary gear sets having manufacturing errors. J Mech Des N Y 139(3):33302
5. Cooley CG, Parker RG (2018) Eigenvalue sensitivity and veering in gyroscopic systems with application to high-speed planetary gears. Eur J Mech A Solids 67:123–136
6. Tsai SJ, Chang LC, Huang CH (2017) Design of cycloid planetary gear drives with tooth number difference of two. Forsch Ingenieurwes 81(2–3):325–336
7. Yang J, Zhang C (2005) Elasto-dynamics of internal gear planetary transmissions. Mech Mach Theory 40(10):1107–1125
8. Huang C, Wang JX, Xiao K et al (2013) Dynamic characteristics analysis and experimental research on a new type planetary gear apparatus with small tooth number difference. J Mech Sci Techol 27(5):1233–1244
9. Li H, Niu W, Zhang D et al (2014) Effect of modification coefficient on nonlinear dynamic characteristics of planetary drive with small teeth number difference. J Vibroengineering 16(1):90–102
10. Dai L, Pu W, Wang J (2018) Mixed EHL analysis of planetary drives with small teeth number difference considering real tooth geometry. Lubr Sci 30(6):317–330
11. Li S (2008) Contact problem and numeric method of a planetary drive with small teeth number difference. Mech Mach Theory 43(9):1065–1086
12. Shu XL (1995) Determination of load sharing factor for planetary gearing with small tooth number difference [J. Mech Mach Theory 30(2):313–321